Journal of Applied Geophysics 176 (2020) 104012

Contents lists available at ScienceDirect

Journal of Applied Geophysics

journal homepage: www.elsevier.com/locate/jappgeo

Soil electrical conductivity imaging using a neural network-based forward solver: Applied to large-scale Bayesian electromagnetic inversion

Davood Moghadas [a,*], Ahmad A. Behroozmand [b], Anders Vest Christiansen [c]

[a] Research Center Landscape Development and Mining Landscapes, Brandenburg University of Technology, D-03046 Cottbus, Germany
[b] Department of Geophysics, Stanford University, Stanford, California, USA
[c] Department of Geoscience, Aarhus University, Aarhus, Denmark

ARTICLE INFO

Article history:
Received 2 January 2020
Received in revised form 27 March 2020
Accepted 1 April 2020
Available online 8 April 2020

Keywords:
Electromagnetic induction
Artificial neural network
Soil electrical conductivity
Bayesian inversion

ABSTRACT

In recent years, probabilistic solution to the inversion of electromagnetic induction (EMI) data has been progressively developed for non-invasive subsurface characterization. However, Bayesian inversion of EMI data using forward solvers based on full solution of Maxwell's equation is associated with computationally expensive modelings, particularly for large-scale surveys. Here, we incorporated artificial neural network (ANN) with Bayesian inference to obtain subsurface electromagnetic conductivity image (EMCI) from EMI data down to 10 m depth. In this respect, a complex EMI forward model was replaced by a trained neural network (ANN proxy forward function) that can be evaluated comparably rapidly. The accuracy of the ANN-based forward solver was examined using different synthetic subsurface models. The proposed methodology was applied on EMI data measured with a DUALEM-421 s sensor from 10 ha study site in the Alken Enge area of Denmark. We compared the inversely estimated EMCI with the counterpart obtained from a quasi-three-dimensional (quasi-3D) spatially-constrained deterministic algorithm as a standard code. The network training procedure was performed within few minutes, and once it was trained, the ANN-based forward solver returned roughly 150,000 model responses per second. This value for the EMI forward solver was around 400, demonstrating the computational efficiency of the ANN proxy forward function. The theoretical simulations demonstrated that the ANN-based forward solver accurately mimics the EMI response within the training range. Moreover, the proposed inversion strategy successfully delineated the subsurface EMCI from Alken Enge area. This approach thus facilitates rapid and accurate subsurface conductivity imaging using Bayesian inversion of multi-configuration EMI data, which is particularly pertinent for large-scale measurements.

1. Introduction

Low frequency electromagnetic induction (EMI) methods have been increasingly used for non-invasive monitoring and characterization of subsurface structures. The rapid measurement capability of this technique facilitates real-time measurements over extended areas (Huang et al., 2015; Martinez et al., 2018). EMI returns apparent electrical conductivity (σ_a or ECa-mS/m) which is the weighted average of the vertical subsurface electrical conductivity (σ-mS/m) distributions, considering a one-dimensional (1D) earth model. The penetration depth of the system is a function of offset (ρ-m) and loop antenna orientation (antenna mode) (Mester et al., 2011; Moghadas et al., 2012). The EMI-obtained information is of great value to solve many different environmental and geotechnical problems (Andre et al., 2012; Triantafilis et al., 2012; Huang et al., 2016; Rejiba et al., 2018; von Hebel et al., 2018). This motivates to develop robust and advanced conductivity imaging techniques for accurate subsurface characterizations using EMI.

In the last decades, numerous approaches have been developed for inversion of ECa data including deterministic (Santos, 2004; Guillemoteau et al., 2012, 2016; Huang et al., 2016; Christiansen et al., 2016) and probabilistic (Minsley, 2011; Shanahan et al., 2015; Jadoon et al., 2017; Moghadas et al., 2017) techniques. Deterministic approach employs optimization algorithms to find a so-called single-best solution and facilitates fast inversion of the data. Probabilistic inversion (e.g. Bayesian inference) returns posterior distribution of the model parameters derived by conditioning the behavior of the model on measurements. In comparison with the deterministic approach, probabilistic inversion provides a richer source of information, since the posterior distribution of the model parameters allows for more efficient uncertainty estimations. The main drawback of the probabilistic inversions is the difficulty to effectively sample the entire parameter space,

* Corresponding author.
E-mail address: moghadas@b-tu.de (D. Moghadas).

https://doi.org/10.1016/j.jappgeo.2020.104012

in particular for high dimensional problems. This, combined with the numerous evaluations of the rigorous forward model make the stochastic sampling algorithms computationally very expensive. The high computational cost of the probabilistic algorithms hampers extensive use of the Bayesian inversions to estimate subsurface geophysical properties, in particular for large-scale surveys. When the number of data is less than that of the unknowns, geophysical inverse problem is under-determined. Unfortunately, multi-layer inversion of EMI data may result in an under-determined problem wherein the sensitivity of the return signal depends in large part on offsets and antenna modes.

Incorporation of dimensionality reduction techniques with the Bayesian inversion facilitates faster convergence of the algorithm and increases the accuracy of the parameter estimations (Jafarpour et al., 2010; Linde and Vrugt, 2013; Laloy et al., 2015). One technique for truncation of the model parameters is discrete cosine transform (DCT). This approach offers a great potential for inversion of many geophysical data types (Linde and Vrugt, 2013; Lochbuhler et al., 2015; Qin et al., 2019a). Recently, Moghadas (2019) proposed to incorporate model compression via DCT with a quasi-two-dimensional (quasi-2D) Bayesian inversion of EMI data. This DCT-based inversion proved to be promising to obtain the subsurface electromagnetic conductivity images (EMCIs) (Moghadas and Vrugt, 2019). Model reduction via DCT can also be coupled with 1D inversion strategies to simplify considerably parameter estimations (Wright et al., 2017).

Along with model compression techniques, machine learning approaches have been increasingly flourished to facilitate the inversion process (Hansen and Cordua, 2017; Giannakis et al., 2019; Conway et al., 2019). In this respect, Hansen and Cordua (2017) proposed a general framework to replace the rigorous geophysical forward evaluation with a trained artificial neural network (ANN) in the probabilistic inversion procedure. The ANN-based forward model equates to the geophysical forward solver but with much lower evaluation time. The algorithm is trained using a large number of randomly generated synthetic subsurface models to construct a trained network that can accurately mimic the functionalities of the forward solver (ANN proxy forward function). Incorporation of the Bayesian inference with the ANN-based forward model is appealing, since it considerably reduces the total computational time required for the convergence of the algorithm. For instance, Hansen and Cordua (2017) demonstrated that a sampling algorithm via ANN-based forward model is three orders of magnitude faster than using 2D ground penetrating radar (GPR) forward solver. Giannakis et al. (2019) also successfully applied ANN proxy modeling for full-waveform inversion of 3D GPR data. Other work by Qin et al. (2019b) examined the feasibility of this approach for transient electromagnetic (TEM) soundings. Most recently, Conway et al. (2019) applied the ANN proxy forward function to the problem of 3D magnetotelluric (MT) inversion.

The ANN-based forward modeling is general and has capacity to considerably change the complexity of non-linear sampling-based inversions for wide variety of geophysical problems. However, the ANN structure for the problem should satisfy the requirements of simplicity and approximation accuracy. For instance, Giannakis et al. (2019) showed that this approach requires to be refined for 3D GPR inversion to well capture the complex antenna-subsurface interactions, combined with ringing noise and losses. For 3D MT surveys, Conway et al. (2019) also reported that classical neural network presents high uncertainties in estimation of regional details compared with the standard MT forward model. They suggested to improve the proxy modeling using more advanced techniques such as convolutional neural networks. Consequently, the relevancy and applicability of the ANN-based forward modeling requires to be examined for each problem considering dimensionality, penetration depth, physics of the problem, etc. To the best of our knowledge, no study exists to examine the feasibility and potential of the ANN proxy modeling for EMI probabilistic inverse problems.

In this paper, we applied a 1D DCT-based inversion to obtain the quasi-three-dimensional (quasi-3D) subsurface EMCI from EMI data measured with a DUALEM-421 s sensor. Drawing inspiration from the work of Hansen and Cordua (2017), we formulated the inverse problem in a Bayesian framework using an ANN-based forward solver for rapid convergence of the routine. The proposed methodology was applied on the EMI data reported by Christiansen et al. (2016) where the measurements were performed in the Alken Enge area of Denmark. We examined the accuracy of the ANN-based forward model via several synthetic scenarios. We juxtaposed the inversely estimated EMCI with the subsurface model obtained by a quasi-3D spatially-constrained deterministic inversion.

2. Materials and methods

2.1. Measurements

This study focuses on 10 ha study site in Alken Enge area of Denmark (Christiansen et al., 2016). The field campaign was launched during a dry period in May 2014. The ECa measurements were performed with a detailed line spacing of around 3 m (varying between 1 and 4 m depending on the accessibility) using a DUALEM-421 s sensor (DualEM, Milton, Ontario, Canada). The sensor was mounted on two non-metallic sledges, enabling real time measurements in the field to characterize the paleo lake shores and related coastal features. Interested readers are referred to Christiansen et al. (2016) for further details regarding the test site, measurement campaign, and data processing.

The DUALEM-421 s sensor allows for ECa measurements using ρ_1=1 m, ρ_2=2 m, and ρ_3=4 m offsets with two coil orientations, namely, horizontal coplanar loops (HCP), and perpendicular loops (PERP). The system operates at 9.0 kHz frequency (diffusive regime). The depth of exploration (DOE) of an EMI system is the depth at which the EMI response is 70% of its sensitivity (Callegary et al., 2007). Based on that, the DOEs of the DUALEM-421 s sensor for PERP configuration are around 0.5-, 1-, and 2-m corresponding to 1-, 2-, and 4-m offsets, respectively. These values are increased to 1.5-, 3-, and 6-m for the corresponding offsets using HCP mode. Data processing resulted to a total number of 13,043 data sets each with 6 ECa values. The data sets for each offset-coil configurations were interpolated to a grid with 100 and 160 cells in horizontal *X* and *Y* directions, respectively using variogram modeling and ordinary kriging. Fig. 1 shows the location of the selected EMI measurement points (blue dots). The gray cells represent the areas considered for the interpolation of the ECa data.

It is important to note that EMI data can be gridded before (Saey et al., 2011; Altdorff et al., 2018) and after (Christiansen et al., 2016) inversion. The original data set used here contained a lot of redundant information which resulted to increase the computation time for the subsequent inversion. As a result, the ECa data were grided before inversion, leading to reduce the total number of data sets from 13,043 to 6682 grid nodes for each of the six coil configurations used in the inversion. The choice of grid size was a trade-off between computational speed and redundant information. Indeed, the electrical conductivity data are often known to have a log-normal distribution (Guillemoteau et al., 2016). To satisfy the normality for variogram analysis, the logarithmic transformation can be applied on the data. Alternatively, one can also formulate the inverse problem in a logarithmic parameter space to better handle the log-normal distribution of electrical conductivity (Guillemoteau et al., 2016). Consequently, here we used a logarithmic parameter space for the electrical conductivity values during the Bayesian inversion.

2.2. 1D DCT-based probabilistic inversion

In this study, we used a so-called full electromagnetic (EM) forward model and mimicked the EMI measurement process at our experimental field site using numerical solutions of the Maxwell equations. Given

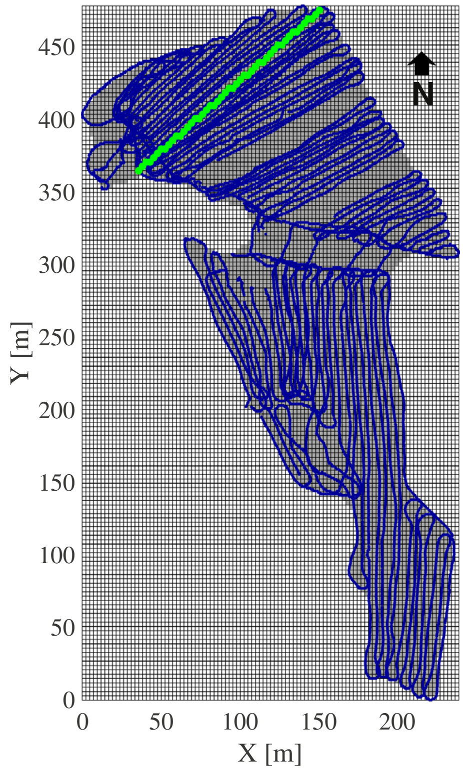

Fig. 1. Location of the EMI measurement points (blue dots) in the study site. The measured ECa values were interpolated to a grid with 100 × 160 cells using ordinary kriging. The gray cells represent the areas considered for the interpolation of the ECa data. The green dots show the selected transect for comparison with the previously inverted data.

1D multi-layered earth, the full EM forward model is formulated as (Wait, 1954; Ward and Hohmann, 1987):

$$\sigma_a^{HCP}(\rho)=\left(\frac{-4\rho}{\omega\mu_0}\right)\ \mathrm{Im}\left[\int_0^\infty R^{TE}\ \exp(-2\lambda h_0)J_0(\rho\lambda)\lambda^2 d\lambda\right]$$
$$\sigma_a^{PERP}(\rho)=\left(\frac{-4\rho}{\omega\mu_0}\right)\ \mathrm{Im}\left[\int_0^\infty R^{TE}\ \exp(-2\lambda h_0)J_1(\rho\lambda)\lambda^2 d\lambda\right], \quad (1)$$

In these expressions, σ_a^{HCP} and σ_a^{PERP} represent measured ECa values in HCP and PERP modes, respectively, ω (rad/s) signifies the angular frequency, μ_0 (m^{-2}) is the free-space permeability, J_0 and J_1 represent zeroth and first-order Bessel functions, respectively, λ (m) is the radial wave number, and h_0 is the height of the instrument above the ground. The transverse electric reflection coefficient, R^{TE} (−) depends on the electrical conductivity and thickness of the layers. To solve eq. (1), we assumed a subsurface model with N=12 layers down to 10 m depth with logarithmically increasing thicknesses (cartesian grid). The last layer was assumed to be a homogeneous half-space. The EMI operating frequency exerts control on the properties of the cartesian grid. With the 9.0 kHz frequency of the DUALEM-421 s sensor, the vertical resolution of the ECa data is rather limited. As a consequence, we used a rather coarse structure of N=12 layers due to the diffusive regime of the EMI field.

There are two measures of the maximum depth of investigation for the EMI sensors on a given model: DOE (McNeill, 1980) which refers to low induction number (LIN) assumption, and depth of investigation (DOI) (Christiansen and Auken, 2012) which is based on the full EM solution. The maximum DOE of a DUALEM-421 s sensor is around 6 m when referring to the LIN approximation (Taylor, 2016). However, Christiansen et al. (2016) demonstrated with synthetic simulations that the estimated maximum depths based on linear assumption may not be accurate. Depending on the subsurface electrical conductivity range, this depth can be lower or higher than DOE, when full solution model is considered. For the Alken Enge field case, Christiansen et al. (2016) showed that the maximum DOI of the sensor can be around 7–9 m in some places which is larger than DOE estimations. As a consequence, the cartesian grid with maximum depth of 10 m considered here is relevant and ensures satisfying the full solution assumptions. Bayesian inversion of 6682 × 6 measured ECa data using EMI forward solver contributes to a CPU-demanding inverse problem. Consequently, we incorporated the Bayesian inversion with model compression via DCT using ANN-based forward solver to increase the accuracy and computational speed of the algorithm, which are discussed in the following sections.

Assuming a subsurface model with n equally spaced layers (regular grid), the DCT is given by (Ahmed et al., 1974):

$$\mathbf{G}(i)=\alpha_i\sum_{z=1}^{n}\mathbf{S}(z)\ \cos\left(\frac{(i-1)\pi(2z-1)}{2n}\right),\quad \alpha_i=\begin{cases}\frac{1}{\sqrt{n}} & \text{if } i=1\\ \sqrt{\frac{2}{n}} & \text{if } 2\le i\le n\end{cases} \quad (2)$$

where z is vertical axis, $i>0$ signifies the column number of the n DCT coefficients of matrix **G** (in frequency domain), and matrix **S** (in space domain) stores values of the electrical conductivity of each DCT grid cell. The matrix **G** contains both low and high frequency components. We considered n=12 cells for the DCT grid. The main information of the DCT stores in the low frequency coefficients (dominant DCT components on the top part of the matrix **G**), i.e., one can recover the original matrix **S** by setting the high frequency components of the matrix **G** to zero and by applying the inverse of the DCT. Linde and Vrugt (2013) showed that an unbiased estimate of the properties of a given inverse problem can be accomplished using appropriate number of dominant DCT coefficients. They suggested to choose this number of DCT coefficient as large as computationally feasible. Wright et al. (2017) showed that around 20% of the total coefficients can be sufficient to establish an accurate 1D DCT-based inversion. Consequently, we defined 5 cells on the top of the matrix **G** for model parametrization. This resulted to have $\theta=\{G(1),\ldots,G(5)\}$ as an unknown model parameter vector, since the remaining high frequency DCT coefficients in the bottom part of matrix **G** were set to zero. Such a model parametrization thus allows for unbiased parameter estimation. Note that the DCT-based model reduction presented in eq. 2 is valid over a regular grid. The 12 estimated conductivity values (matrix **S**) were then interpolated to the cartesian grid (irregular grid) to compute the forward response.

Incorporation of the Bayesian inference with model compression via DCT offers several advantages. Instead of performing the stochastic sampling in the full parameter space (a 12 layered model), we assumed that the model properties can be sufficiency described with a much lower dimensionality. Estimation of the 12 subsurface electrical conductivity values contributes to an under-determined problem, since the DUALEM-421 s sensor returns 6 multi-configuration ECa values. While DCT reduces the number of model parameters to 5, providing an over-determined inverse problem. Moreover, the low frequency coefficients of the DCT store the main transform information in such a way that the first component contains the maximum information content. Such a capability provides an effective way for assigning the lower and upper parameter ranges to better guide the search algorithm for convergence (Linde and Vrugt, 2013; Moghadas and Vrugt, 2019). This considerably simplifies posterior exploration in comparison with classical parameter estimations in space domain (Linde and Vrugt, 2013). Note that here we are not dealing with a high dimensional inverse problem, since estimation of 12 conductivity values does not lead to a high computational burden for the algorithm. Nevertheless, integration of the

DCT with the Bayesian inference not only helps to cast the Bayesian framework as an over-determined problem, but also better assists the selection of prior information compared with inversion of the original 12 parameters. We will revisit this topic at a later stage.

To inversely estimate unknown parameters, θ, we employed a sampling routine via Differential Evolution Adaptive Metropolis algorithm (DREAM) developed by Vrugt et al. (2009). We used $\mathrm{DREAM}_{(zs)}$ (Laloy and Vrugt, 2012) which is based on original DREAM algorithm, but requires only 3 chains for convergence. This algorithm rapidly explores target distributions by running several Markov chains simultaneously in parallel for T generations. Convergence of the sampled chains is monitored using the $\hat{R}$ statistic of Gelman and Rubin (1992), which compares the within-chain and between-chain variance of each parameter. Convergence can be declared if $\hat{R}\leq 1.2$ for each parameter, otherwise a larger number of generations, T, is required. Interested readers are referred to Laloy and Vrugt (2012) for detailed description of the $\mathrm{DREAM}_{(zs)}$ algorithm. The DREAM software package in MATLAB (Vrugt, 2016) was used for our experiment using $T=5000$ and default values of the algorithmic variables.

Given ν the total number of offsets, the ECa values of HCP and PERP modes for each measurement point were grouped together to construct a 2ν vector of ECa values. The log-likelihood function, $l(\theta)$, is formulated as:

$$l(\theta) = -\frac{(2\nu)}{2}\ \ln\left(\sum_{k=1}^{2\nu} e_k^2(\theta)\right) \tag{3}$$

In this expression, $e_k(\theta) = \sigma_a^{meas}(k) - \sigma_a^{mod}(k,\theta)$ is the ECa residuals in which σ_a^{meas} and σ_a^{mod} are measured and modeled multi-configuration ECa vectors, respectively. Eq. 3 presents a Gaussian likelihood that assumes residual errors, $e(\theta)$, are to be independent and to be described by a normal probability distribution with a mean of zero and a constant variance. The root mean square error (RMSE) between the measured and modeled data is formulated by:

$$RMSE = \sqrt{\frac{1}{2\nu}\sum_{k=1}^{2\nu}\left[\sigma_a^{meas}(k) - \sigma_a^{mod}(k)\right]^2} \tag{4}$$

To define the prior information, we first adjusted the minimum (σ_{min}) and maximum (σ_{max}) conductivity ranges between 2 mS/m and 100 mS/m, respectively. Afterwards, we determined the upper and lower bounds of each elements of θ as follows. First, $\mathbf{G}(1)$ was scaled in such a way that the inverse DCT of $\mathbf{G}(1)$ was between $\log(\sigma_{min})$ and $\log(\sigma_{max})$ (the values of $\mathbf{G}(1)$ contains the maximum information about the transform). The remaining elements were scaled in a similar way so that after the inverse transform each component had a corresponding value of $\log((\sigma_{max} - \sigma_{min})/2)$ (Linde and Vrugt, 2013).

As mentioned, we formulated the inverse problem in a logarithmic parameter space to better handle the log-normal distribution of electrical conductivity. It is worth noting that geostatistical prior modeling also assists to improve the scaling of the low frequency components in particular, for a multi-dimensional DCT-based Bayesian inference (Lochbuhler et al., 2015; Moghadas and Vrugt, 2019). We assumed uniform prior distributions for the unknown model parameters. Since the parameter space was defined in the frequency domain, the search algorithm may produce some subsurface models with conductivity values outside the specified range of $2 - 100$ mS/m during the inversion. For such proposals, a very low likelihood value was assigned to automatically discard them. The DCT-based inversion of the Alken Enge data sets resulted to 6682 depth-profile electrical conductivity models (1D models) which were stitched together to build a quasi-3D EMCI.

It is important to reiterate that a probabilistic solution to an inverse problem is presented as a posterior distribution. Here, we summarized the results of our Bayesian inference as maximum a posteriori probability (MAP), mean of the posterior (MEAN), and 95% confidence interval of the posterior distribution. The confidence interval assists to investigate the uncertainty estimation and is defined as the difference between 2.5 and 97.5 percentiles of the posterior distribution. The Bayesian inference appropriately treats the nonlinearity of the model and adequately characterize parameter uncertainties. However, with increasing the number of unknown parameters, the probability of the prior in the vicinity of the posterior will typically decrease (Rosas-Carbajal et al., 2014). Moreover, the use of an inadequate prior distribution can produce unrealistic models and increases the ill-posedness of the Bayesian inverse problem (Rosas-Carbajal et al., 2014; Moghadas and Vrugt, 2019). Comparison between MAP and MEAN solutions facilitates to explore the well-posedness of the probabilistic inversion, as well as appropriate selection of the prior information (Moghadas and Vrugt, 2019).

Christiansen et al. (2016) applied a deterministic routine to invert the measured ECa values using EMI forward solver based on full solution of the Maxwell's equation. The maximum depth of the domain was fixed to 10 m considering a subsurface model similar to the cartesian grid used here. This non-linear inversion approach was originally developed by Auken et al. (2015) and employs a quasi-3D spatially-constrained algorithm (Viezzoli et al., 2008). Here, we denote the inversion results of the Christiansen et al. (2016) as “Deterministic”.

2.3. ANN-based forward modeling

Now we have defined the different building blocks of the DCT-based Bayesian framework, we are left with the ANN-based forward modeling. ANN is a supervised machine learning technique applied to extract the patterns and relationships in data using a conceptual model of the human brain. The learning and adaptive capacity of the ANN algorithm makes it appealing for solving many different geophysical problems (van der Baan and Jutten, 2000; Hansen and Cordua, 2017; Moghadas and Badorreck, 2019). The ANN architecture is constructed based on three different neurons including input (), hidden layer, and output (). The input signals are assembled as numerically expressed information. They are weighted based on their degree of importance (activation numbers). After summation of these signals, they are transferred among different nodes based on their activation number. The activation continues through the entire neural network, until it reaches the output layer. We considered a feed-forward ANN using a single hidden layer. The Bayesian regularization back-propagation algorithm was also employed to robustly capture the non-linear features of the EMI model. A sigmoid and linear activation function was used for the hidden and output layers, respectively.

To create an ANN-based forward solver, first we randomly generated $ND=20{,}000$ subsurface models down to 10 m depth with discretizations ($N=12$ layers) similar to the cartesian grid (an $\mathrm{N} \times \mathrm{ND}$ matrix of conductivity values). We assumed a conductivity range of $2 - 100$ mS/m, corresponding to the lower and upper bounds of the search space in our Bayesian inversion. Latin hypercube sampling (LHS) method (McKay et al., 2000) was used to generate the training models considering uniform distribution. The LHS approach applies stratification of the parameter probability distributions by dividing the cumulative curve into equal intervals on the cumulative probability scale. A sample is then randomly taken from each interval of the distribution. This preserves randomness and independence of the samples and avoids unwanted correlation between parameters. We calculated the forward responses (eq. 1) for all ND random models considering both HCP and PERP modes, resulted to generate a $6 \times \mathrm{ND}$ matrix of multi-configuration ECa values. Then, the input and output layers for the ANN were constructed as:

$$\Psi = \begin{bmatrix} \sigma_{1,1} & \cdots & \sigma_{1,ND} \\ \vdots & \vdots & \vdots \\ \sigma_{N,1} & \cdots & \sigma_{N,ND} \end{bmatrix}, \Phi = \begin{bmatrix} \sigma_{a,1}^{HCP}(\rho_1) & \cdots & \sigma_{a,ND}^{HCP}(\rho_1) \\ \sigma_{a,1}^{HCP}(\rho_2) & \cdots & \sigma_{a,ND}^{HCP}(\rho_2) \\ \sigma_{a,1}^{HCP}(\rho_3) & \cdots & \sigma_{a,ND}^{HCP}(\rho_3) \\ \sigma_{a,1}^{PERP}(\rho_1) & \cdots & \sigma_{a,ND}^{PERP}(\rho_1) \\ \sigma_{a,1}^{PERP}(\rho_2) & \cdots & \sigma_{a,ND}^{PERP}(\rho_2) \\ \sigma_{a,1}^{PERP}(\rho_3) & \cdots & \sigma_{a,ND}^{PERP}(\rho_3) \end{bmatrix} \tag{5}$$

Fig. 2 presents the schematic of the ANN structure used to simulate the EMI forward response. We considered the first 60% of the data as a training, the second 20% as a validation, and the last 20% as a test set. The training data was utilized to calculate the weights and biases during the learning procedure. The errors on the validation data set were regularly monitored to ensure optimal performance of the ANN algorithm. The test subset was employed to provide an unbiased control over the network to avoid over- and under-fitting.

Optimal selection of the number of neurons (j) in the hidden layer plays an important role in ANN architecture. To find the appropriate number of neurons, we used a trial method based on optimal performance. In this regard, the training networks with $j = 1, 2, \ldots, 10$ number of neurons in the hidden layer were developed with the same inputs and outputs. We found that the network with 7 neurons have the best performance to fully capture the complexity of the system. The whole network training procedure required a total computational time of around 3 min, presenting the computational efficiency of the training stage for ANN proxy forward modeling. During the Bayesian inversion, the search algorithm generates different realistic and unrealistic proposals to be accepted or rejected by the algorithm. As a result, it is important that the ANN to be provided with a sufficient set of training models to perform generalization and to accurately mimic the functionality of the EMI forward solver during the inversion.

Here, we randomly generated the training models from latin hypercube sampling, considering a uniform distribution with flexible spatial variability for 12 subsurface conductivity values. The proposed Bayesian inversion strategy solved the problem with 5 low frequency coefficients considering uniform prior for the DCT components. However, generating the DCT coefficients from a uniform prior does not necessarily lead to the spatial components with the same probability distributions. This may be a source of modeling errors during the Bayesian inference. Indeed, the use of ANN proxy forward solver results in a modeling error bias. Hansen and Cordua (2017) demonstrated that by increasing the size of the training set, the modeling error related to using ANN-based

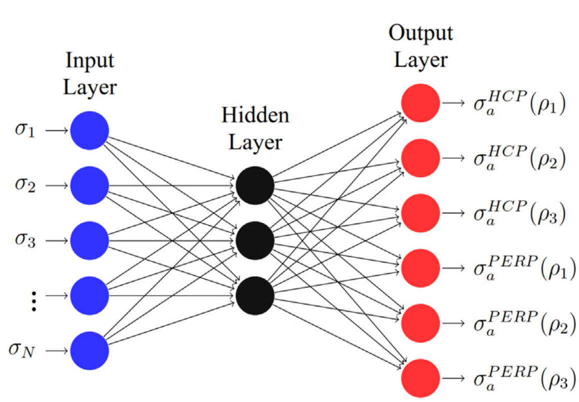

Fig. 2. Schematic of the ANN structure used to simulate the EMI forward response. The subsurface electrical conductivity ($\sigma_1, \sigma_2, \ldots, \sigma_N$) values were considered as inputs. The output targets were the simulated multi-configuration ECa values from DUALEM-421 s sensor.

forward function decreases. For simplicity, we selected a large sample size for network training and assumed that errors in the ANN-based forward solver were randomly distributed as suggested by Conway et al. (2019). Alternatively, one can further improve the inversion results by quantifying the modeling errors such that it can be accounted for during the Bayesian inference based on the methodology proposed by Hansen et al. (2014). It is important to note that the ANN training can be performed on the prior of the low frequency DCT components. Such a proxy modeling requires to generate a large DCT components in frequency domain. However, transforming the coefficients to the spatial domain generates a large number of out of range subsurface models. This complicates appropriate definition of the training models within the stipulated conductivity range. As a result, the network training was performed on the 12 layered subsurface electrical conductivity models.

We examined the robustness and accuracy of the trained network using four different synthetic subsurface multi-layered conductivity models. The models were randomly generated considering 12 layers with logarithmically increasing thicknesses down to 10 m depth. These depth-profile structures, hereafter referred to as Model 1–4, are presented in Fig. 3. Model 1 mimics a subsurface structure with conductivity range of 2–100 mS/m. This range corresponds to the lower and upper bounds used for training the network. Model 2 and Model 3 represent a relatively low (2–30 mS/m) and relatively high (70–100 mS/m) conductivity range. These two scenarios were designed to examine if the ANN-based forward solver is able to accurately simulate the subsurface responses for relatively extreme resistive/conductive structures within the training range. Model 4 with conductivity range of 50–350 mS/m considers a scenario in which the conductivity range is broken such that the neural network does not have training knowledge for some parts of the conductivity space.

To further examine the accuracy of the ANN-based proxy modeling using DCT parametrization, we inversely estimated electrical conductivity values from Models 1–3. Two inversion scenarios were considered. The first approach (Inversion 1) corresponded to the coupled DCT-based Bayesian inference with ANN-based forward solver using 5 dominant DCT coefficients as unknown parameters. The second scenario (Inversion 2) considered the inversion of 12 electrical conductivity values using EMI forward solver. Note that we applied no truncation for the second inversion and considered the lower and upper parameter ranges between 2 mS/m and 100 mS/m, respectively for all 12 parameters. These two synthetic inversion scenarios were designed to demonstrate the interest of model compression for a low dimensional 1D EMI inversion, and to explore the accuracy of the ANN-based forward model for the Bayseian inference.

3. Results

3.1. ANN results

The ANN algorithm was trained using the synthetic multi-configuration ECa data generated from 20,000 random subsurface models. Fig. 4 presents the calculated forward responses from four different subsurface synthetic models with increasing offset on the x-axis. The theoretical simulations were carried out using HCP (blue lines) and PERP (red lines) modes. The solid and dashed lines represent the calculated ECa values using Maxwell-based EMI forward model (eq. 1) and ANN-based forward solver, respectively.

Regrading Model 1 (Fig. 4 (a)), the ANN-based results agree with their counterparts calculated using eq. 1. The total RMSE is around 0.07 mS/m, indicating excellent performance of the neural network in the presence of subsurface conductivity ranges where the training procedure was implemented. For both models 2 and 3 (Fig. 4 (b-c)), the trained network successfully simulated the subsurface responses with total RMSEs less than around 0.3 mS/m. This confirms the robustness of the ANN-based forward solver to accurately mimic the EMI forward

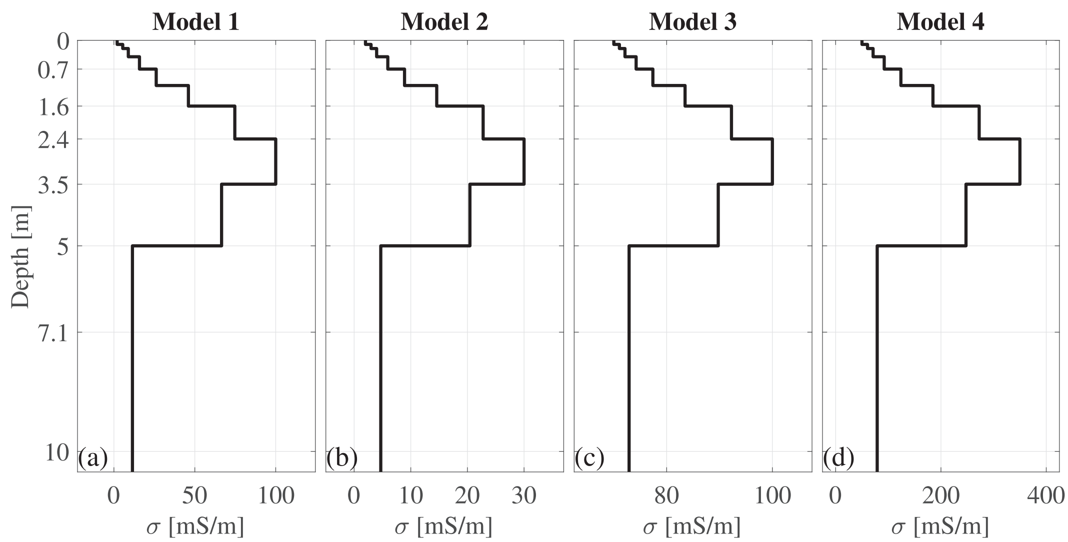

Fig. 3. 1D synthetic subsurface multi-layered models with conductivity range of: a) 2–100 mS/m (Model 1); b) 2–30 mS/m (Model 2); c) 70–100 mS/m (Model 3); and d) 50–350 mS/m (Model 4). Each model consists of 12 layers with logarithmically increasing thicknesses down to 10 m depth. These depth-profile electrical conductivity models were used to compare the responses between the EMI (eq. 1) and ANN-based forward solvers.

response considering different complex subsurface features. Regarding Model 4 (Fig. 4 (c)), the ANN-based responses present some discrepancies with those calculated by EMI forward model (RMSE = 7.07 mS/m). The last scenario shows that the ANN-based forward model should be retrained for delineation of subsurface conductivity features that lie outside the stipulated training ranges, which consequently need to match the expected electrical conductivity distribution of the investigated test site. The synthetic simulations presented here demonstrated that the ANN proxy function equates to the Maxwell-based EMI forward solver. This ensures an accurate estimate of the properties of a given EMI Bayesian inverse problem within the ANN training range.

To compare the evaluation time of the forward modeling routines, we determined the total number of possible forward simulations per second using ANN-based and EMI forward solvers. We considered the

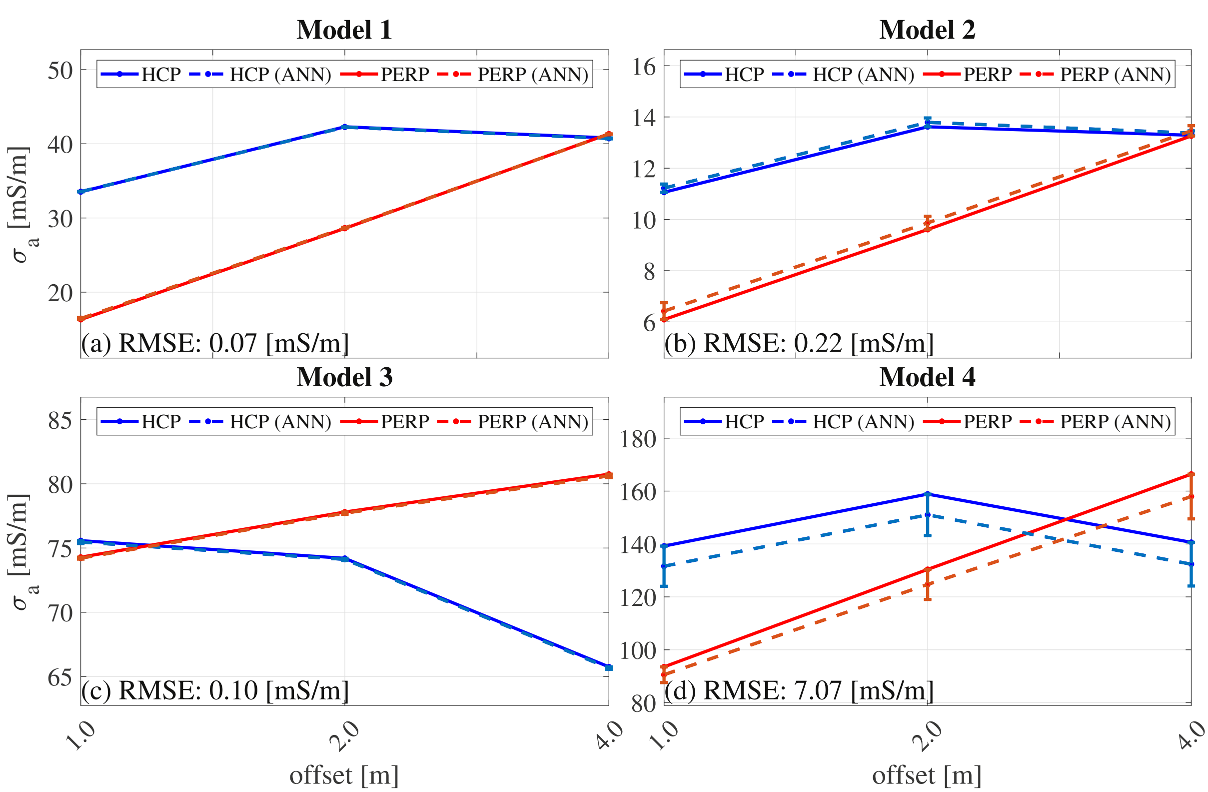

Fig. 4. Calculated forward responses from HCP (blue lines) and PERP (red lines) modes using a) Model 1; b) Model 2; c) Model 3; and d) Model 4. The solid and dashed lines represent the calculated ECa values using EMI (eq. 1) and ANN-based forward solvers, respectively.

synthetic model presented in Fig. 3(a) for the simulations. Note that our EMI forward solver is a built-in C MEX file which is called from MATLAB. The trained network is also a MATLAB function which was converted to a C MEX file to further accelerate the evaluation process and to have consistency of comparison with the EMI forward solver. The simulations were carried out on one core of an office PC (system: Intel(R) Core(TM) i7–6700 CPU, 3.40 GHz, 16,0 GB RAM). The EMI forward solver computes roughly 400 model responses per second. This value is increased to around 150,000 using ANN-based forward solver, demonstrating the superior computational efficiency of the neural network for 1D modeling, once the network is trained.

To further illustrate the computational efficiency of the neural network, we repeated the simulations considering 50 subsurface models together. These simulations are of strong practical relevance and can mimic quasi-2D EMI modeling frameworks using ECa transect measurements. Given a 1D earth model, a quasi-2D EMI inversion requires to discretize the subsurface domain of the transect in a large number of grid cells. The conductivity of each grid cell is then determined by fitting the data to the modeled ECa values calculated by incorporating all 1D subsurface models along the transect together (Moghadas and Vrugt, 2019). The second set of simulations benefited as well from parallel computing (on four separate threads) for EMI forward calculations. The EMI forward solver computed roughly 10 model responses per second and for 50 subsurface profiles together using parallel computing. For such a scenario, the ANN-based forward solver returned around 70,000 models per second without parallelization. The synthetic simulations presented here thus manifest the computational efficiency of the neural network in comparison with the EMI forward model and ensure rapid multi-configuration ECa calculations.

3.2. Inversion results: synthetic data

Fig. 5 shows the inversely estimated subsurface electrical conductivity profiles using a-c) DCT-based Bayesian inference with ANN proxy forward function; d-f) Bayesian inversion of 12 electrical conductivity values with EMI forward model. The first, second, and third columns present the results from synthetic Model 1, 2, and 3, respectively. The black, red, and blue lines represent the synthetic subsurface model, MAP, and MEAN solutions, respectively. The gray areas show the 95% confidence interval of the posterior distributions. The RMSE between

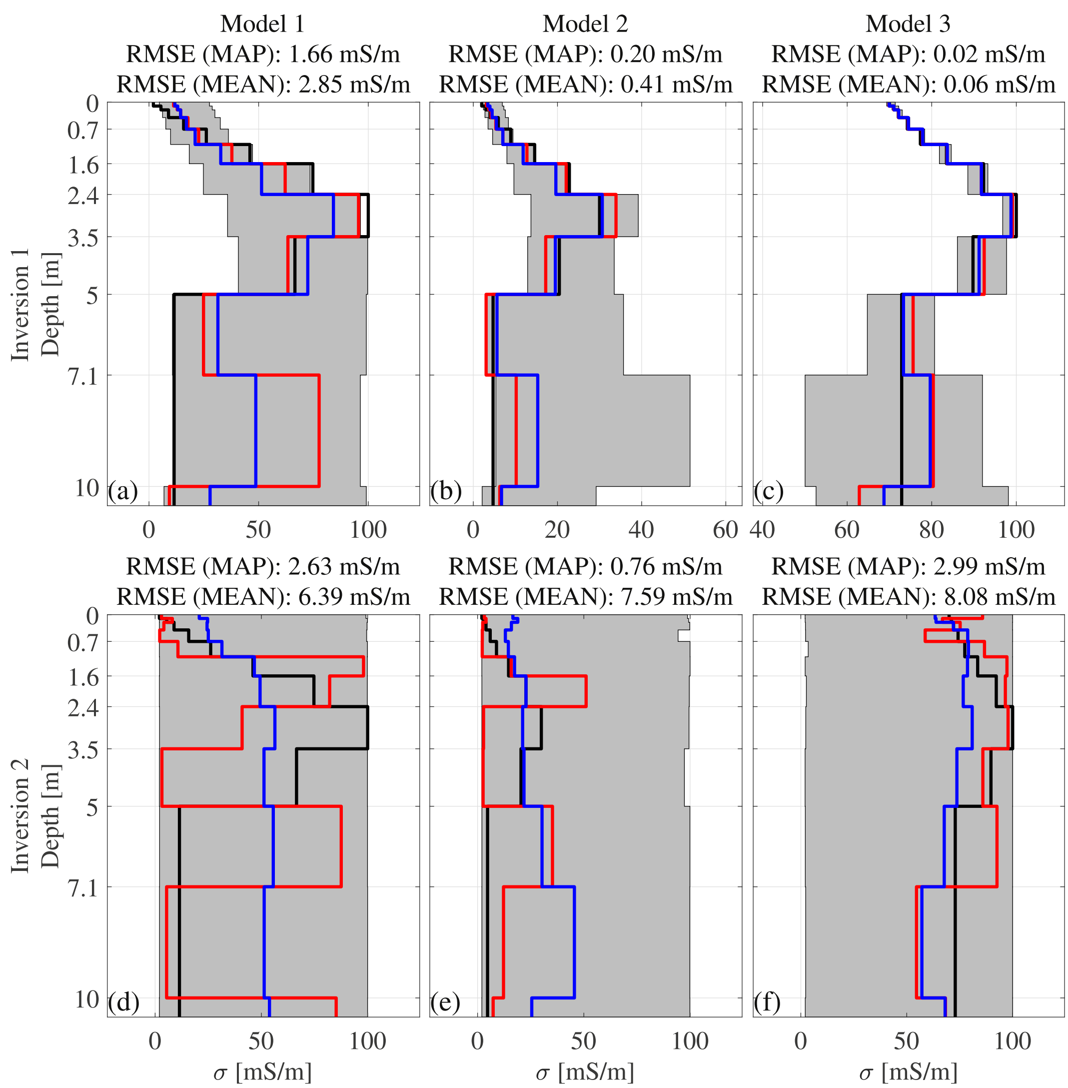

Fig. 5. Inversely estimated subsurface electrical conductivity profiles using a-c) DCT-based Bayesian inference with ANN proxy forward function; d-f) Bayesian inversion of 12 electrical conductivity values with EMI forward model. The first, second, and third columns present the results from synthetic Model 1, 2, and 3, respectively. The black, red, and blue lines represent the synthetic subsurface model, MAP, and MEAN solutions, respectively. The gray areas represent the 95% confidence interval of the posterior distributions. The RMSE between the synthetic and modeled ECa data obtained from MAP solution is shown by RMSE (MAP). The corresponding value from MEAN solution is presented by RMSE (MEAN).

the synthetic and modeled ECa data obtained from MAP solution is shown by RMSE (MAP). The corresponding value from MEAN solution is presented by RMSE (MEAN).

In the first place, notice the superiority of the first inversion results compared with those obtained from the second scenario. The RMSE values of Inversion 1 are less than their counterparts from Inversion 2. Regarding the DCT-based inversion of Model 1 (Fig. 5(a)), some discrepancies between the syntectic, MAP and MEAN solutions can be seen. This is because Model 1 considers larger conductivity contrasts in comparison with the two other models. The disagreement between the inversely estimated and the synthetic models are more pronounced for deeper layers, where the EMI field presents lower sensitivity. The estimated conductivities for the second and third models (Fig. 5(b-c)) are in agreement with the synthetic values (the RMSEs are less than 0.5 mS/m).

The second inversion scenario resulted to irrelevant subsurface models with large RMSEs up to around 8 mS/m. A large discrepancy between the synthetic models, MAP and MEAN solutions is observed. The reasons for superiority of the first inversion than the second scenario are two folds. First, Inversion 1 and 2 considered 5, and 12 unknown model parameters, respectively, incorporating 6 ECa values. As a result, the first inversion was formulated in an over-determined framework, while the second scenario was under-determined. Second, the first inversion benefited from scaling of DCT elements, providing better guide for the search algorithm to converge in comparison with the Inversion 2 that considered the same prior ranges for all parameters. Comparison between the 95% confidence intervals of the two Bayesian inversion scenarios clearly confirm this claim. This study further demonstrated the accuracy of the ANN-based forward modeling for inversion of multi-configuration ECa data.

3.3. Inversion results: experimental data

The measured multi-configuration ECa values were inverted for all 6682 data sets using coupled DCT-based Bayesian inversion and ANN-based forward solver. The total evaluation time was around 12 h using one core of the office PC. Fig. 6 shows the quasi-3D subsurface EMCIs obtained from a) deterministic approach, b) MAP solution, and c) MEAN solution. Fig. 6(d) also presents the 95% confidence interval of the posterior distribution. These results highlight several important findings. First, a close agrement between the MAP and MEAN solutions can be seen. This manifests the well-possedness of the inverse problem with the posterior conductivity image that remains in close vicinity of the MAP solution. Second, despite consistency between the Bayesian and deterministic solutions, there are some discrepancies between them. Moreover, the deterministic approach provided a more smoothed subsurface EMCI in comparison with the Bayesian inversion results. This is not unexpected since the deterministic algorithm employs spatially-constrained technique. Despite that, both methodologies resolved almost similar subsurface features. Third, the 95% confidence interval of the posterior distribution appears rather small close to the surface and tends to increase deeper in the domain. This is due to the fact that the sensitivity of the EMI decreases by increasing the depth. Consequently, using the irregular parametrization for calculating the forward response (cartesian grid) appears more desirable over a regular one, since it introduces higher resolution cells on the top of the domain (Moghadas, 2019).

Fig. 7 presents the inversion results in terms of probability distribution (P_d [%]) plots for a) deterministic, b) MAP, c) MEAN, and d) 95% confidence interval. The probability distribution diagrams assist to evaluate the overall variations of subsurface conductivity as a function of depth and facilitate a more elaborative comparison between different inversion scenarios (Behroozmand et al., 2019). These probability distributions were calculated by aggregating the inversely estimated electrical conductivity values of all soundings for each depth.

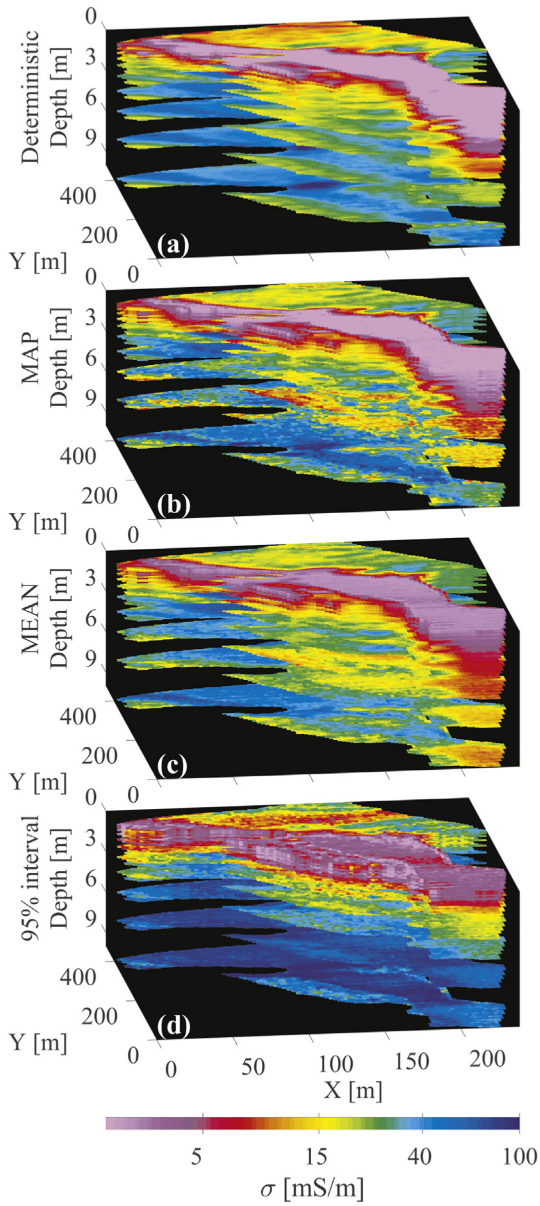

Fig. 6. a) Subsurface EMCI abstained from the deterministic approach (Christiansen et al., 2016); DCT-based Bayesian inversion results: b) maximum a posteriori probability (MAP); c) mean of the posterior distribution (MEAN); d) 95% confidence interval of the posterior solution.

Regarding the deterministic approach (Fig. 7(a)), two conductivity zones with conductivity ranges of 2–10 mS/m ($P_d > 70\%$) and 20–50 mS/m ($P_d \simeq 40\%$) within the 0–1.6 m depth can be observed. As we will see later, these zones are representative of a sandy structure for the shallow layers. The depth interval of 1.6–2.4 m reveals two zones with conductivity ranges of around 2–20 mS/m and 20–50 mS/m, representing sand and organic silt, respectively. The conductivity distribution diagram presents a conductivity between 10 and 30 mS/m for 2.4–3.5 m depth. For layers deeper than 3.5 m, the minimum of the conductivity is around 20 mS/m. The maximum conductivity starts from around 35 mS/m and increases downwards up to around 50 mS/m. The deterministic solution, MAP (Fig. 7(b)) and MEAN (Fig. 7(c)) of the posterior distributions demonstrate almost similar P_d patterns for the corresponding layers despite some small discrepancies. These differences are more pronounced for the layers deeper than 5 m since the sensitivity of the EMI signal is considerably impaired in deeper

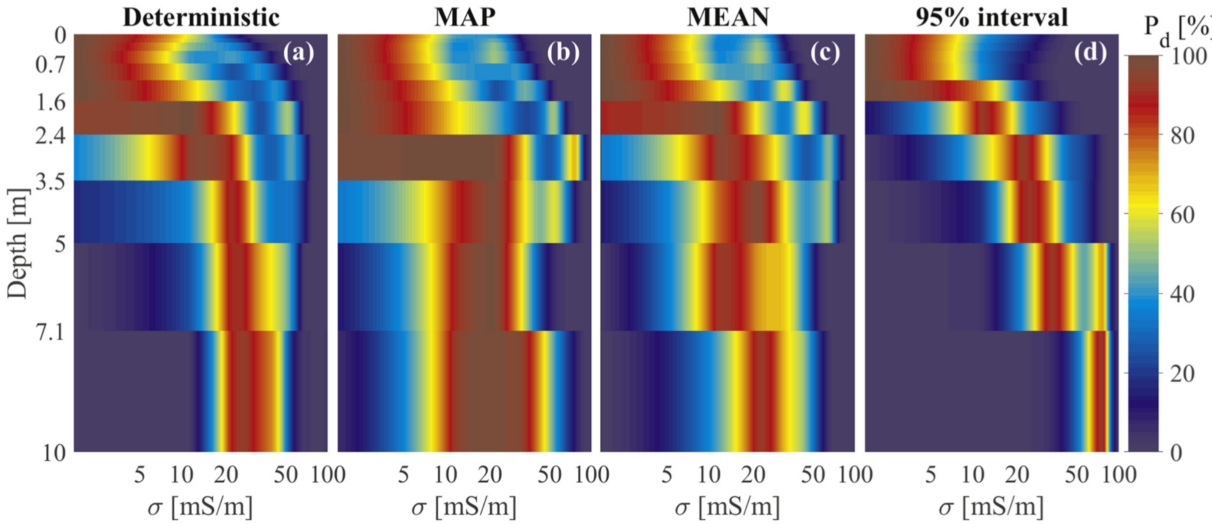

Fig. 7. Probability distribution (P_d [%]) plots obtained from a) deterministic solution (Christiansen et al., 2016); b) MAP; c) MEAN; and d) 95% confidence intervals.

parts of the domain. The 95% confidence interval (Fig. 7(d)) is relatively small close to the surface and tends to increase downwards since the EMI depth sensitivity is a function of depth.

Fig. 8 shows the map of RMSE values between the measured and modeled data calculated using a) deterministic results, b) MAP, and c) MEAN, respectively. All scenarios show acceptable overall performances of the inversions by total RMSEs less than 2 mS/m. However, some points suffer from over-fitting which is due to the fact that the Gaussian log-likelihood function (eq. 3) does not include any regularization term.

3.4. Geological interpretations

Fig. 9 compares the inversion results as a cross-section corresponding to the selected transect in Fig. 1. This transect was located in the vicinity of the borehole surveys (Christiansen et al., 2016). Fig. 9 (a) presents the RMSE between the measured and modeled ECa values. Fig. 9(b-e) show the deterministic solution, MAP, MEAN, and confidence interval, respectively. The DOI obtained from the deterministic inversion is denoted by a dashed line. Note that DOI provides a more accurate estimation of the depth sensitivity than DOE (Christiansen et al., 2016).

The RMSE values (Fig. 9 (a)) demonstrate the rather well performances of all scenarios. These results reconfirm our previous inference regarding the well-posedness of the Bayesian approach since the MAP and MEAN images show almost similar subsurface patterns. The confidence interval is also small close to the surface and tends to increase downwards. Although the deterministic and Bayesian results are in close agreement, some discrepancies can be observed between them. For $X > 30$ m, the MAP solution (Fig. 9 (c)) shows some conductivity bounds (15–20 mS/m) around 6 m depth. However, the deterministic routine provides a smooth conductivity model due to the lateral and vertical constraints. The conductivity bounds were not appeared in the subsurface model based on the mean of the posterior distribution. This area is located bellow the DOI values where the EMI does not have enough sensitivity. These cross-sections highlight several small-scale geological features of the archeological importance. Near the beginning of the transect ($X < 30$ m), a low conductive region ($\sigma < 10$ mS/m) is

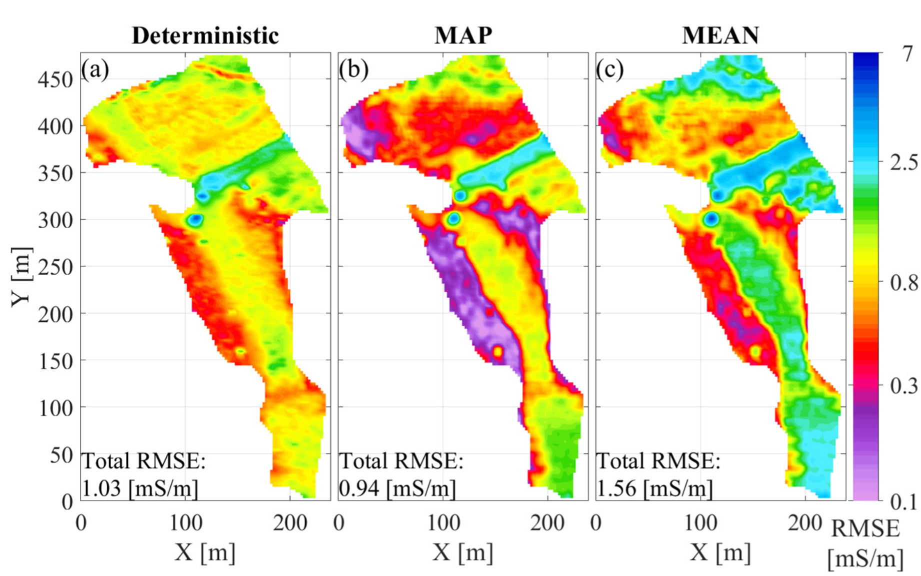

Fig. 8. The map of RMSE values between the measured and modeled data calculated using a) deterministic results (Christiansen et al., 2016); b) MAP; and c) MEAN, respectively.

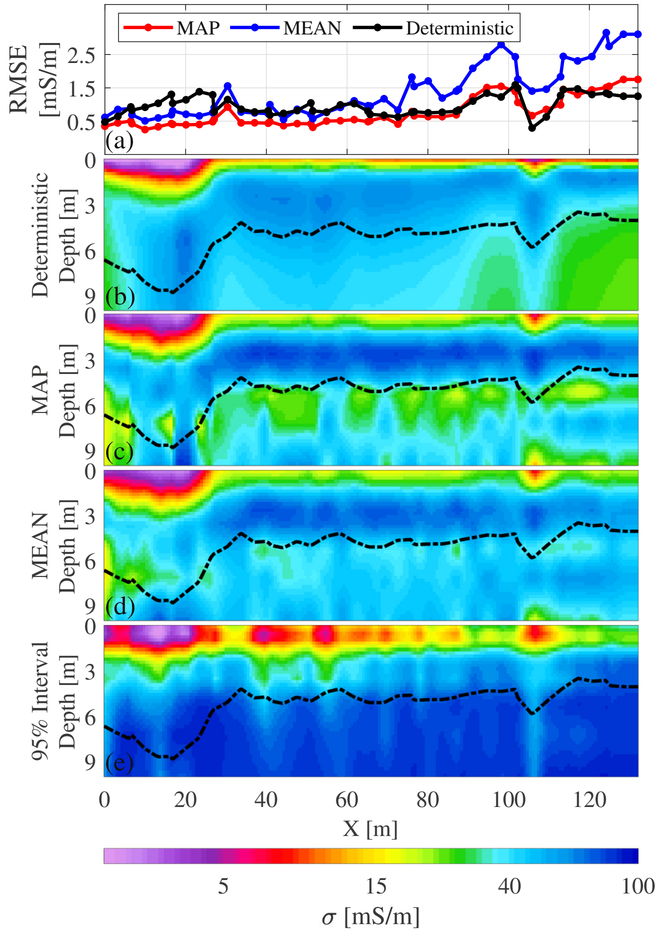

Fig. 9. Comparison between the inversion results corresponding to the selected transect (Fig. 1) obtained from the deterministic (Christiansen et al., 2016) and probabilistic inversions: a) RMSE values b) deterministic solution; c) MAP; d) MEAN; and e) confidence interval of the posterior distribution. The dashed line denotes the depth of investigation (DOI) calculated from the deterministic inversion.

found on the top of the domain down to around 2 m depth. Previous borehole excavations reported by Christiansen et al. (2016) suggests the sandy structure for this unit. Moreover, after $X=100$ m, a conductive zone with σ around 10 mS/m (the small red spot) is observed which is attributed to the Paleo stream channel. The rest of the sections reveal a dry peat sediments with electrical conductivity range of 10–25 mS/m close to the surface with around 30 cm thickness. Below the shallow sand/peat layer, the lake sediments and organic rich silts are found as high conductive regions (25–100 mS/m).

We calculated the mean electrical conductivity ($\overline{\sigma}$) maps for two depth-intervals of 0–1 m, and 1–2 m which are presented in Fig. 10. For simplicity, we considered 4 different regions on the maps denoted by A1-A4. Mean conductivity/resistivity plan view maps are commonly used to present the subsurface geophysical models at specific depth intervals. Previous investigations based on borehole measurements (Christiansen et al., 2016) suggest the presence of dry peat for the 0–1 m interval. Moreover, the Paleo stream channel appears as a yellow-red bound on the top of the A1 area. Regarding the 1–2 m depth interval, the estimated $\overline{\sigma}$ structures are attributed to organic silt (A1), dry peat (A2, and A4), and sand (A3). Furthermore, the inversely estimated maps with the Bayesian inference are in a close agreement with their counterpart from the deterministic inversion. Regarding the A3 region, the Bayesian inversion presents rather high uncertainties for parameter estimations since the MAP and MEAN solutions provide relatively different conductivity values.

4. Discussion

Before we move on to the conclusion section, we would like to discuss and reiterate a few key points that may be of practical concern and/or importance. In this study, the lower and upper bounds used for generating the random subsurface conductivity models for ANN training were selected in such a way to include a relatively large range (2–100 mS/m). According to our theoretical simulations, for forward and/or inverse modelings outside this range, the ANN algorithm with a larger range should be retrained to mimic the functionality of the forward solver for the new range. Hansen and Cordua (2017) showed that the number of randomly selected models should be larger than 5000 to build a trained network that can accurately mimic the geophysical forward response. Indeed, assigning the appropriate number of training models to accomplish an acceptable network performance depends on a specific application. Nevertheless, a rough rule of thumb is to train a neural network with a data set larger than 5000 samples for effective generalization of the problem (Puzyrev, 2019). Consequently, the 20,000 generated random models is adequate and ensures an accurate ANN-based forward modeling.

The ANN-based forward solver used here was trained based on a 12 layered subsurface model. Selection of the number of subsurface layers is a trade-off between model complexity and resolution. A dense discretized grid introduces more input parameters for the neural network to be related to the forward response. Training a network to accurately mimic the EMI response based on such a dense subsurface layering structure requires a more complex ANN architecture. Nevertheless, the use of a dense grid for EMI inversion does not necessarily improve the results, since the EMI operates in the diffusive regime and vertical resolution of the ECa data is somewhat limited. Consequently, the choice of a rather coarse grid is adequate for accurate subsurface imaging from EMI data. This simplifies considerably the training procedure to build an ANN-based forward solver.

We juxtaposed the result of our proposed inversion strategy with the subsurface model obtained by the quasi-3D spatially-constrained algorithm used by Christiansen et al. (2016). The results demonstrated that there are relatively small discrepancies between the two approaches for 1D electrical conductivity modeling, presenting a rather quasi-linear problem. Yet, the use of Bayesian inversion for subsurface imaging from multi-configuration EMI data can be a preferable choice. The reasons are two folds. First, convergence of the deterministic method is highly sensitive to the initial model. Second, Bayesian inference provides uncertainty of the posterior distribution which is more informative than the single best estimation of the deterministic solution. Moghadas and Vrugt (2019) showed that appropriate selection of the prior distribution for DCT-based probabilistic EMI inversion significantly improve the results with posterior mean that remains in close vicinity of the MAP solution. Here, appropriate choice of the prior information (DCT coefficients in frequency domain) provided posterior distribution with reduced variance. It is worth noting that a significant effort has been made to develop full 3D EM forward solutions. For instance, Guillemoteau and Tronicke (2016) developed a fast 3D modeling algorithm formulated in the hybrid spectral-spatial domain for loop-loop EMI systems. Guillemoteau et al. (2017) also successfully validated this methodology using field data measured by a DUALEM21 sensor. Here, the multi-configuration EMI measurements were carried out with a line spacing varying between 1 and 4 m. Given the DUALEM421 inter-coil spacings, such a data acquisition strategy makes the relocation of the anomalies between the adjacent lines rather complicated. As a consequence, we assumed that 1D forward modeling was appeared sufficient to model spatial variations of the electrical conductivity, since the measurement meshing was not sufficiently small to perform a full 3D inversion.

The use of an ANN proxy forward modeling opens up a wide-arsenal of probabilistic inversions for large-scale subsurface characterizations. This is particularly important in the present context as Bayesian

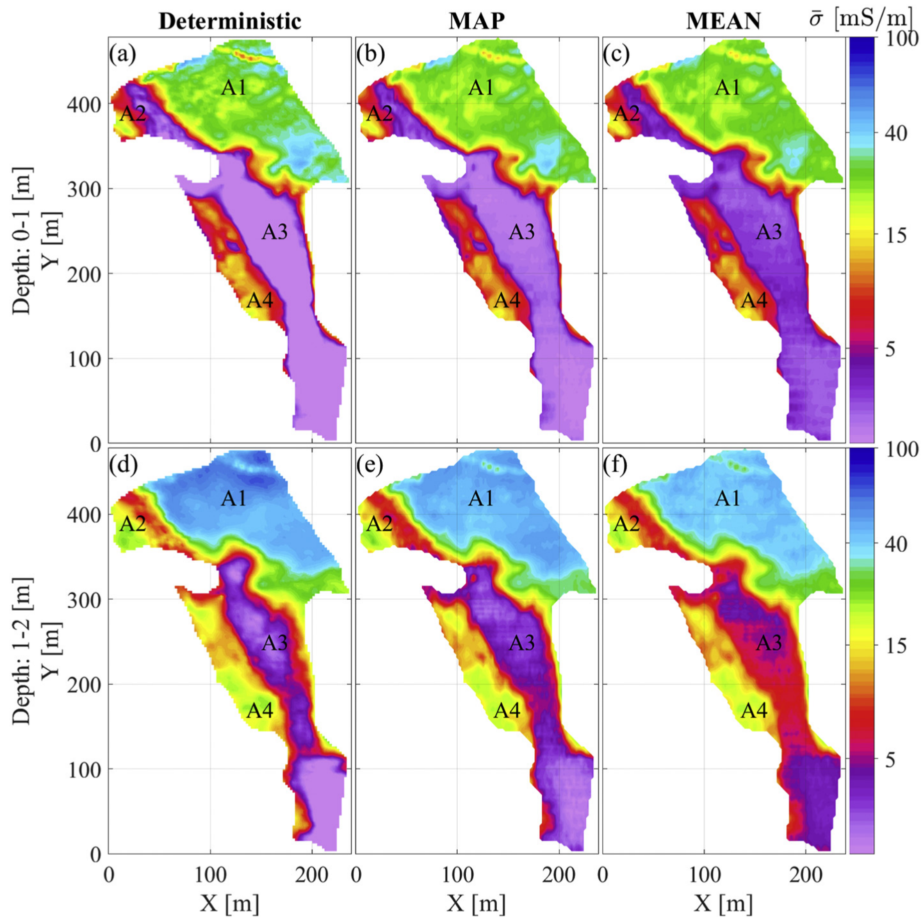

Fig. 10. Mean electrical conductivity ($\overline{\sigma}$) maps in a depth of 0–1 m (first row) and 1–2 m (second row). The first, second, and third columns correspond to the deterministic solution (Christiansen et al., 2016), MAP, and MEAN of the posterior distributions, respectively. The A1-A4 denote different regions on the maps.

inversions are often associated with computationally expensive modelings. The applicability of this approach can be also extended to the other existing geophysical methods such as airborne techniques for rapid and accurate multi-dimensional subsurface modelings from large-scale measurement.

5. Conclusion

In this paper, we coupled DCT-based Bayesian inversion of the multi-configuration ECa data with the ANN approach for rapid and accurate delineation of the subsurface structures. We applied this methodology to invert the ECa data collected over the 10 ha study site in the Alken Enge area of Denmark. This study demonstrated that the EMI forward model based on full solution of Maxwell's equations can be successfully replaced by a trained neural network. The ANN algorithm translates the complex nonlinear relationships between different elements of the EMI forward model to the weights and biases in the trained network. Such a proxy forward function is even faster than parallel computation of the EMI forward model. This is particularly desirable for the Bayesian inversion of ECa data for large-scale surveys using full-solution forward solver, since this approach requires rigorous evaluations of the model. Moreover, the trained network demonstrated a well performance for resistive/conductive features within the training range. However, in the presence of the subsurface conductivity structures where the ANN-based forward solver does not have training knowledge, the network should be retrained with new conductivity ranges. Coupled DCT-based Bayesian inference and neural network for large data set inversion from Alken Enge area manifested the computational efficiency and accuracy of the proposed approach. This methodology thus appears promising for large-scale subsurface electrical conductivity imaging using multi-configuration EMI measurements.

Acknowledgments

This work was supported by the Brandenburg University of Technology Cottbus - Senftenberg (BTU, Germany). Jasper A. Vrugt (University of California Irvine) is acknowledged for providing the DREAM package. The constructive comments by Julien Guillemoteau (University of Potsdam), two anonymous reviewers, editor, Mark E. Everett (Texas A&M University), and associate editor, Thomas Günther (Leibniz institute for applied geophysics) assisted to improve the manuscript which are acknowledged.

MATLAB codes of the proposed ANN proxy forward modeling strategy are available from the author and can be downloaded from https://github.com/ML4Geophysics/ANN-Based-Forward.

References

Ahmed, N., Natarajan, T., Rao, K.R., 1974. Discrete cosine transform. IEEE Trans. Comput. 23 (1), 90–93. https://doi.org/10.1109/t-c.1974.223784 C.

Altdorff, D., Galagedara, L., Nadeem, M., Cheema, M., Unc, A., 2018. Effect of agronomic treatments on the accuracy of soil moisture mapping by electromagnetic induction. CATENA 164, 96–106. https://doi.org/10.1016/j.catena.2017.12.036.

Andre, F., van Leeuwen, C., Saussez, S., Van Durmen, R., Bogaert, P., Moghadas, D., de Resseguier, L., Delvaux, B., Vereecken, H., Lambot, S., 2012. High-resolution imaging of a vineyard in south of France using ground-penetrating radar, electromagnetic induction and electrical resistivity tomography. J. Appl. Geophys. 78, 113–122. https://doi.org/10.1016/j.jappgeo.2011.08.002.

Auken, E., Christiansen, A.V., Kirkegaard, C., Fiandaca, G., Schamper, C., Behroozmand, A.A., Binley, A., Nielsen, E., Efferso, F., Christensen, N.B., Sorensen, K., Foged, N., Vignoli, G., 2015. An overview of a highly versatile forward and stable inverse algorithm for airborne, ground-based and borehole electromagnetic and electric data. Explor. Geophys. 46 (3), 223–235. https://doi.org/10.1071/eg13097.

Behroozmand, A.A., Auken, E., Knight, R., 2019. Assessment of managed aquifer recharge sites using a new geophysical imaging method. Vadose Zone J. 18 (1). https://doi.org/10.2136/vzj2018.10.0184.

Callegary, J.B., Ferre, T.P.A., Groom, R.W., 2007. Vertical spatial sensitivity and exploration depth of low-induction-number electromagnetic-induction instruments. Vadose Zone J. 6 (1), 158–167. https://doi.org/10.2136/vzj2006.0120.

Christiansen, A.V., Auken, E., 2012. A global measure for depth of investigation. Geophysics 77 (4), WB171–WB177.

Christiansen, A.V., Pedersen, J.B., Auken, E., Soe, N.E., Holst, M.K., Kristiansen, S.M., 2016. Improved geoarchaeological mapping with electromagnetic induction instruments from dedicated processing and inversion. Remote Sens. 8 (12), 15. https://doi.org/10.3390/rs8121022.

Conway, D., Alexander, B., King, M., Heinson, G., Kee, Y., 2019. Inverting magnetotelluric responses in a three-dimensional earth using fast forward approximations based on artificial neural networks. Comput. Geosci. 127, 44–52. https://doi.org/10.1016/j.cageo.2019.03.002.

Gelman, A., Rubin, D.B., 1992. Inference from iterative simulation using multiple sequences. Stat. Sci. 7 (4), 457–472. https://doi.org/10.1214/ss/1177011136.

Giannakis, I., Giannopoulos, A., Warren, C., 2019. A machine learning-based fast-forward solver for ground penetrating radar with application to full-waveform inversion. IEEE Trans. Geosci. Remote Sens., 1–10 https://doi.org/10.1109/TGRS.2019.2891206.

Guillemoteau, J., Tronicke, J., 2016. Evaluation of a rapid hybrid spectral-spatial domain 3D forward modeling approach for loop-loop electromagnetic induction quadrature data acquired in low-induction number environments. Geophysics 81 (6), E447–E458. https://doi.org/10.1190/geo2015-0584.1.

Guillemoteau, J., Sailhac, P., Behaegel, M., 2012. Fast approximate 2D inversion of airborne TEM data: born approximation and empirical approach. Geophysics 77 (4), WB89–WB97. https://doi.org/10.1190/geo2011-0372.1.

Guillemoteau, J., Simon, F.X., Luck, E., Tronicke, J., 2016. 1D sequential inversion of portable multi-configuration electromagnetic induction data. Near Surf. Geophys. 14 (5), 423–432. https://doi.org/10.3997/1873-0604.2016029.

Guillemoteau, J., Christensen, N.B., Jacobsen, B.H., Tronicke, J., 2017. Fast 3D multichannel deconvolution of electromagnetic induction loop-loop apparent conductivity data sets acquired at low induction numbers. Geophysics 82 (6), E357–E369. https://doi.org/10.1190/geo2016-0518.1.

Hansen, T.M., Cordua, K.S., 2017. Efficient Monte Carlo sampling of inverse problems using a neural network-based forward-applied to GPR crosshole traveltime inversion. Geophys. J. Int. 211 (3), 1524–1533. https://doi.org/10.1093/gji/ggx380.

Hansen, T.M., Cordua, K.S., Jacobsen, B.H., Mosegaard, K., 2014. Accounting for imperfect forward modeling in geophysical inverse problems - exemplified for crosshole tomography. Geophysics 79 (3), H1–H21. https://doi.org/10.1190/geo2013-0215.1.

Huang, J., Taghizadeh-Mehrjardi, R., Minasny, B., Triantafilis, J., 2015. Modeling soil salinity along a hillslope in Iran by inversion of EM38 data. Soil Sci. Soc. Am. J. 79 (4), 1142–1153. https://doi.org/10.2136/sssaj2014.11.0447.

Huang, J., Scudiero, E., Clary, W., Corwin, D.L., Triantafilis, J., 2016. Time-lapse monitoring of soil water content using electromagnetic conductivity imaging. Soil Use Manag. https://doi.org/10.1111/sum.12261.

Jadoon, K.Z., Altaf, M.U., McCabe, M.F., Hoteit, I., Muhammad, N., Moghadas, D., Weihermuller, L., 2017. Inferring soil salinity in a drip irrigation system from multi-configuration EMI measurements using adaptive Markov chain Monte Carlo. Hydrol. Earth Syst. Sci. 21 (10), 5375–5383. https://doi.org/10.5194/hess-21-5375-2017.

Jafarpour, B., Goyal, V.K., McLaughlin, D.B., Freeman, W.T., 2010. Compressed history matching: Exploiting transform-domain sparsity for regularization of nonlinear dynamic data integration problems. Math. Geosci. 42 (1), 1–27. https://doi.org/10.1007/s11004-009-9247-z.

Laloy, E., Vrugt, J.A., 2012. High-dimensional posterior exploration of hydrologic models using multiple-try DREAM((ZS)) and high-performance computing. Water Resour. Res. 48. https://doi.org/10.1029/2011wr010608.

Laloy, E., Linde, N., Jacques, D., Vrugt, J.A., 2015. Probabilistic inference of multi-gaussian fields from indirect hydrological data using circulant embedding and dimensionality reduction. Water Resour. Res. 51 (6), 4224–4243. https://doi.org/10.1002/2014wr016395.

Linde, N., Vrugt, J.A., 2013. Distributed soil moisture from crosshole ground-penetrating radar travel times using stochastic inversion. Vadose Zone J. 12 (1), 16. https://doi.org/10.2136/vzj2012.0101.

Lochbuhler, T., Vrugt, J.A., Sadegh, M., Linde, N., 2015. Summary statistics from training images as prior information in probabilistic inversion. Geophys. J. Int. 201 (1), 157–171. https://doi.org/10.1093/gji/ggv008.

Martinez, G., Huang, J., Vanderlinden, K., Giraldez, J.V., Triantafilis, J., 2018. Potential to predict depth specific soil water content beneath an olive tree using electromagnetic conductivity imaging. Soil Use Manag. https://doi.org/10.1111/sum.12411.

McKay, M.D., Beckman, R.J., Conover, W.J., 2000. A comparison of three methods for selecting values of input variables in the analysis of output from a computer code. Technometrics 42 (1), 55–61.

McNeill, J.D., 1980. Electromagnetic Terrain Conductivity Measurement at Low Induction Numbers. Tech note TN-6. Geonics Ltd, Mississauga, ON, Canada.

Mester, A., van der Kruk, J., Zimmermann, E., Vereecken, H., 2011. Quantitative two-layer conductivity inversion of multi-configuration electromagnetic induction measurements. Vadose Zone J. 10 (4), 1319–1330. https://doi.org/10.2136/vzj2011.0035.

Minsley, B.J., 2011. A trans-dimensional bayesian markov chain Monte Carlo algorithm for model assessment using frequency-domain electromagnetic data. Geophys. J. Int. 187 (1), 252–272. https://doi.org/10.1111/j.1365-246X.2011.05165.x.

Moghadas, D., 2019. Probabilistic inversion of multiconfiguration electromagnetic induction data using dimensionality reduction technique: a numerical study. Vadose Zone J. 18 (1). https://doi.org/10.2136/vzj2018.09.0183.

Moghadas, D., Badorreck, A., 2019. Machine learning to estimate soil moisture from geophysical measurements of electrical conductivity. Near Surf. Geophys. 17 (2), 181–195. https://doi.org/10.1002/nsg.12036.

Moghadas, D., Vrugt, J.A., 2019. The influence of geostatistical prior modeling on the solution of DCT-based bayesian inversion: a case study from chicken creek catchment. Remote Sens. 11 (13), 1549. https://doi.org/10.3390/rs11131549.

Moghadas, D., Andre, F., Bradford, J.H., van der Kruk, J., Vereecken, H., Lambot, S., 2012. Electromagnetic induction antenna modelling using a linear system of complex antenna transfer functions. Near Surf. Geophys. 10 (3), 237–247. https://doi.org/10.3997/1873-0604.2012002.

Moghadas, D., Jadoon, K.Z., McCabe, M.F., 2017. Spatiotemporal monitoring of soil water content profiles in an irrigated field using probabilistic inversion of time-lapse EMI data. Adv. Water Resour. 110, 238–248. https://doi.org/10.1016/j.advwatres.2017.10.019.

Puzyrev, V., 2019. Deep learning electromagnetic inversion with convolutional neural networks. Geophys. J. Int. 218 (2), 817–832. https://doi.org/10.1093/gji/ggz204.

Qin, H., Xie, X., Tang, Y., 2019a. Evaluation of a straight-ray forward model for bayesian inversion of crosshole ground penetrating radar data. Electronics 8 (6), 630.

Qin, S., Wang, Y., Xu, Z., Liao, X., Liu, L., Fu, Z., 2019b. Fast resistivity imaging of transient electromagnetic using ANN. IEEE Geosci. Remote Sens. Lett., 1–5 https://doi.org/10.1109/LGRS.2019.2900992.

Rejiba, F., Schamper, C., Chevalier, A., Deleplancque, B., Hovhannissian, G., Thiesson, J., Weill, P., 2018. Multiconfiguration electromagnetic induction survey for paleochannel internal structure imaging: a case study in the alluvial plain of the river seine, France. Hydrol. Earth Syst. Sci. 22 (1), 159–170. https://doi.org/10.5194/hess-22-159-2018.

Rosas-Carbajal, M., Linde, N., Kalscheuer, T., Vrugt, J.A., 2014. Two-dimensional probabilistic inversion of plane-wave electromagnetic data: Methodology, model constraints and joint inversion with electrical resistivity data. Geophys. J. Int. https://doi.org/10.1093/gji/ggt482.

Saey, T., Van Meirvenne, M., Dewilde, M., Wyffels, F., De Smedt, P., Meerschman, E., Islam, M.M., Meeuws, F., Cockx, L., 2011. Combining multiple signals of an electromagnetic induction sensor to prospect land for metal objects. Near Surf. Geophys. 9 (4), 309–317. https://doi.org/10.3997/1873-0604.2010070.

Santos, F.A.M., 2004. 1-D laterally constrained inversion of EM34 profiling data. J. Appl. Geophys. 56 (2), 123–134. https://doi.org/10.1016/j.jappgeo.2004.04.005.

Shanahan, P.W., Binley, A., Whalley, W.R., Watts, C.W., 2015. The use of electromagnetic induction to monitor changes in soil moisture profiles beneath different wheat genotypes. Soil Sci. Soc. Am. J. 79 (2), 459–466. https://doi.org/10.2136/sssaj2014.09.0360.

Taylor, R., 2016. Apparent Conductivity as an Indicator of Thickness. Available. online http://www.dualem.com/acit.htm.

Triantafilis, J., Wong, V., Santos, F.A.M., Page, D., Wege, R., 2012. Modeling the electrical conductivity of hydrogeological strata using joint-inversion of loop-loop electromagnetic data. Geophysics 77 (4), WB99–WB107.

van der Baan, M., Jutten, C., 2000. Neural networks in geophysical applications. Geophysics 65 (4), 1032–1047. https://doi.org/10.1190/1.1444797.

Viezzoli, A., Christiansen, A., Auken, E., Sørensen, K., 2008. Quasi-3D modeling of airborne TEM data by spatially constrained inversion. Geophysics 73 (3), F105–F113. https://doi.org/10.1190/1.2895521.

von Hebel, C., Matveeva, M., Verweij, E., Rademske, P., Kaufmann, M.S., Brogi, C., Vereecken, H., Rascher, U., van der Kruk, J., 2018. Understanding soil and plant interaction by combining ground based quantitative electromagnetic induction and airborne hyperspectral data. Geophys. Res. Lett. 45 (15), 7571–7579. https://doi.org/10.1029/2018gl078658.

Vrugt, J.A., 2016. Markov chain Monte Carlo simulation using the DREAM software package: Theory, concepts, and MATLAB implementation. Environ. Model. Softw. 75, 273–316. https://doi.org/10.1016/j.envsoft.2015.08.013.

Vrugt, J.A., Braak, C.J.F., Robinson, B.A., Hyman, J.M., Higdon, D., 2009. Accelerating markov chain monte carlo simulation by differential evolution with self-adaptive randomized subspace sampling. Int.l J.f Nonlinear Sci. Numeri. Simul. 10 (3), 273–290.

Wait, J.R., 1954. Mutual coupling of loops lying on the ground. Geophysics 19 (2), 290–296.

Ward, S.H., Hohmann, G.W., 1987. Electromagnetic theory for geophysical application. In: Nabighian, M.N. (Ed.), Electromagnetic Methods in Applied Geophysics, Investigations in Geophysics Series. 1. Society of Exploration Geophysicists, Tulsa, OK. ISBN: 978-1-56080-263-1, pp. 131–312.

Wright, A., Walker, J.P., Robertson, D.E., Pauwels, V.R.N., 2017. A comparison of the discrete cosine and wavelet transforms for hydrologic model input data reduction. Hydrol. Earth Syst. Sci. 21 (7), 3827–3838. https://doi.org/10.5194/hess-21-3827-2017.